Application of a three-dimensional viscous transonic inverse method to NASA rotor 67

W T Tiow* and **M Zangeneh**
Department of Mechanical Engineering, University College London, UK

Abstract: The development and application of a three-dimensional inverse methodology in which the blade geometry is computed on the basis of the specification of static pressure loading distribution is presented. The methodology is based on the intensive use of computational fluid dynamics (CFD) to account for three-dimensional subsonic and transonic viscous flows. In the design computation, the necessary blade changes are determined directly by the discrepancies between the target and initial values, and the calculation converges to give the final blade geometry and the corresponding steady state flow solution. The application of the method is explored using a transonic test case, NASA rotor 67. Based on observations, it is conclusive that the shock formation and its intensity in such a high-speed turbomachinery flow are well defined on the loading distributions. Pressure loading is therefore as effective a design parameter as conventional inverse design quantities such as static pressure. Hence, from an understanding of the dynamics of the flow in the fan in relation to its pressure loading distributions, simple guidelines can be developed for the inverse method in order to weaken the shock formation. A qualitative improvement in performance is achieved in the redesigned fan. The final flowfield result is confirmed by a well-established commercial CFD package.

Keywords: inverse design, pressure loading, turbomachinery, blades

NOTATION

AGARD	Advisory Group for Aerospace Research and Development
NASA	National Aeronautics and Space Administration, USA
N	number of blades in the cascade arrangement
P	static pressure
rV_θ	swirl velocity (radius multiplied by tangential velocity)
(r, θ, z)	cylindrical polar coordinates
Re	Reynolds number
s	blade pitch
t_θ	tangential blade thickness (rad)
V	absolute velocity
$\alpha^{\pm}$	angular offset of a point on the upper (+) and lower (−) surfaces of a blade
Δ	difference in the flow value between two reference points
ΔP	pressure difference between the upper (+) and lower (−) surfaces of a blade at a given axial position (design parameter)
(ξ, η)	body-fitted coordinate system
ω	rotational speed

Subscripts

bl	average flow values on the upper and lower surfaces of a blade at a given position
$i$slip	value calculated based on satisfying the slip (tangency) flow condition
J	transformation jacobian (r, z) to (ξ, η)
j_{stack}	stacking position: fixed camber geometry

Superscripts

m	original value of surface pressures before the specified ΔP is imposed
$m+1$	new value of surface pressures after the specified ΔP is imposed
n	nth design iteration
0	initial value
1	first approximation
+	value on the upper surface of a blade

The MS was received on 16 July 2001 and was accepted after revision for publication on 12 February 2002.

**Corresponding author: Department of Mechanical Engineering, University College London, Torrington Place, London WC1E 7JE, UK.*

$-$	value on the lower surface of a blade
$*$	target value (used to denote the specified design value)
$\sim$	mass-average

1 INTRODUCTION

The advances of computational techniques in flow analysis have been tremendous in the last decade. Complemented by increasing computing power, it is now common to use a variety of three-dimensional solver codes for routine design [**1**]. Based on computational fluid dynamics (CFD) results, successive blade modifications are usually performed in order to achieve an ideal flow pattern. The conventional blade design practice is based on empirical methods combined with the experience of specialist designers. Recently, radical new methods have emerged, and their principles suggest that blade optimization may be achieved in a more theoretical and logical manner.

One new class of design methods is usually referred to as *inverse methodology*. In this approach, the blade geometry is computed directly from the specification of a required flow parameter. Existing two- and three-dimensional inverse methods are formulated with different design parameters. Popular inverse design specifications for blade/cascade designs include the distributions of surface static pressure [**2–4**] and averaged mean swirl (radius multiplied by tangential velocity, rV_θ) [**5–7**]. The successful use of the latter in practical blade designs has been reported in several studies. These include the suppression of secondary flows [**8**], improving pump suction performance [**9**] and the design of high-performance marine ducted propulsors [**10**, **11**].

The success of the inverse design methodology in practical applications has been its ability to allow designers to use their fluid dynamics insights directly in improving a design. The systematic approach taken by the inverse methods provide the important link between design intent and blade geometry.

More sophisticated inverse methodologies are now being developed that are based on advanced CFD techniques. At the most advanced level, the method has shock capturing ability and can cope in subsonic and transonic, viscous flow. Demeulenaere *et al.* [**12**] reported an extension of their method to the design of two-dimensional compressor cascades in viscous flow. Tiow and Zangeneh [**13**] coupled a three-dimensional viscous flow solver with a design algorithm based on the mass-averaged swirl velocity to give a simple inverse procedure. The methodology was applied successfully for the designs of both turbine and fan blades in high transonic viscous flows. Recently, three-dimensional inverse approaches have been extended to include the specification of static pressure loading (i.e. surface static pressure difference between the blade upper and lower surfaces). By specifying the ΔP distribution together with the tangential thickness, it is possible to control the blade pressure loading directly, which is very important in controlling shock losses in transonic/supersonic flow and cavitation in incompressible flow, while maintaining structurally sound blades. Furthermore, the ΔP specification can be readily used in three dimensions. The initial development of this methodology in two dimensions was covered in earlier work [**14**] and separately in references [**15**] and [**16**]. More recent applications of this method are reported in references [**17**] and [**18**].

In this article, the development and application of the authors' three-dimensional inverse method based on pressure loading specification are described. The proposed method essentially solves the full three-dimensional Euler equations, and the design algorithm has been formulated to include the explicit specification of the blade tangential thickness and thus has the ability to cope with thick profiles. To account for viscosity, the Euler solution has also been improved by adding a viscous loss simulation using the log law and the mixing length models. A transonic fan blade, NASA rotor 67, is redesigned to illustrate the design methodology.

2 DESCRIPTION OF THE EULER FLOW SOLVER: ANALYSIS AND DESIGN MODE

Finite volume analysis of the three-dimensional unsteady Euler equations is used. The unsteady flow equations are discretized with respect to the cylindrical polar coordinates (r, θ, z) and are solved for steady solution.

Viscous effects are included using the log law and mixing length models (descriptions in the next section), and the effect of blade rotation is also modelled. The developed solver uses a cell vertex [**19**] approach and an adopted central difference scheme with added dissipation and a multistage Runge–Kutta integrator [**20**]. Local time stepping and grid sequencing have been implemented in the present computer code to accelerate convergence.

The developed solver may be used in either the *direct analysis* or the *design* mode. The main differences in the solver operating in these two modes are primarily in the implementation of the boundary conditions. These are described in section 2.2.

2.1 Modelling of viscous effects

The motivation to include viscous effects in Euler solutions stems directly from the fact that the computation of full Navier–Stokes solution in an iterative fashion, as in an inverse design cycle, is expensive. However, it is risky completely to neglect the viscous effects, and thus the inclusion of dissipative forces in inviscid solution is not uncommon. Denton [**21**] proposed the possibility of simple modelling using body force, where the dissipative stresses are computed directly from the classical skin friction coefficient. Despite being completely empirical, the approximation leads to realistic results. Denton [**22**] reported an improved extension of the work where the dissipative forces are determined using the mixing length model. The

latter is implemented here to model viscous losses. It is acknowledged that the modelling of viscous effects in the solver described here is based entirely on the method proposed by Denton [**22**]. It is also noted that the viscous modelling employed here is intermediate between being fully viscous and inviscid where the surface flow is allowed to slip along the solid walls. The model produces many of the details of real viscous flows but is very economical in terms of the number of cells required to achieve reasonable flow resolution. These are the prime considerations in the development of the current method.

2.2 Boundary conditions: analysis and design mode

In the cascade calculation, four different types of boundary are required: inlet, outlet, solid walls and periodicity. At the inlet, the total pressure and temperature profiles and two absolute flow directions in the streamwise and meridional plane are specified. The static pressure is extrapolated from the interior flowfield domain, which is used in conjunction with the isentropic relation to calculate the density and velocity. At the downstream boundary, the exit static pressure is held fixed on the hub and the radial variation is obtained via the radial equilibrium conditions.

A periodic or a cyclic condition is imposed to model the symmetry of flow between each sector of the cascade. This condition is applied upstream of the leading edge and downstream of the trailing edge where the values at two corresponding points are set to be equal.

In the analysis mode, the solid surfaces of the blade, including the shroud and hub walls, are represented by imposing zero normal convective fluxes. The surface flow therefore satisfies the tangency condition and slips along the surfaces. In the design mode, the tangency condition is not imposed on the blade surfaces. In this case, the blade wall allows convective fluxes and the surfaces are modelled as *permeable* or *transpiring*. Details of the transpiration model are given in section 3.

2.3 Analysis validations

The solutions of the developed Euler solver (in analysis mode) with viscous modelling are first validated using a transonic fan. This example is taken from AGARD Advisory Report 275 [**23**] catalogued specifically for validation of computational results. The flow of the rotor 67 transonic fan is highly three-dimensional and viscous and has been used by several researchers to verify their viscous solutions [**24–26**].

Vertical sheared H-grid topology is used to generate the computational domain, and the computation is carried out under conditions corresponding to the rotor operating near its peak efficiency. The comparisons of total pressure, total temperature and flow angle at the rotor inlet (Aero Station 1) and/or outlet survey stations (Aero Station 2) with the experiments are shown in Figs 1 to 3 respectively. As shown in Fig. 1, along the exit survey station, good correlation of the total pressure ratio is observed with the

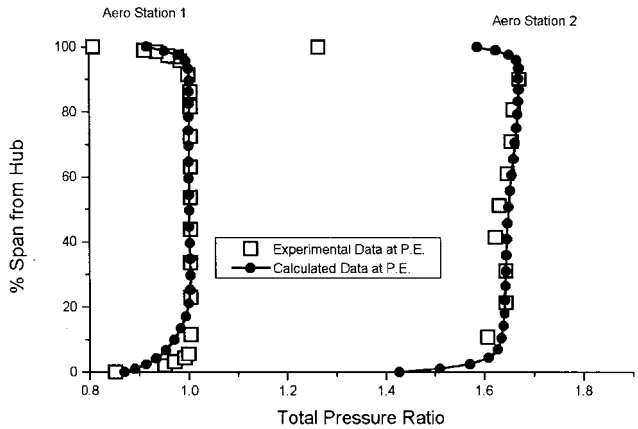

Fig. 1 Total pressure profiles at Aero Stations 1 and 2

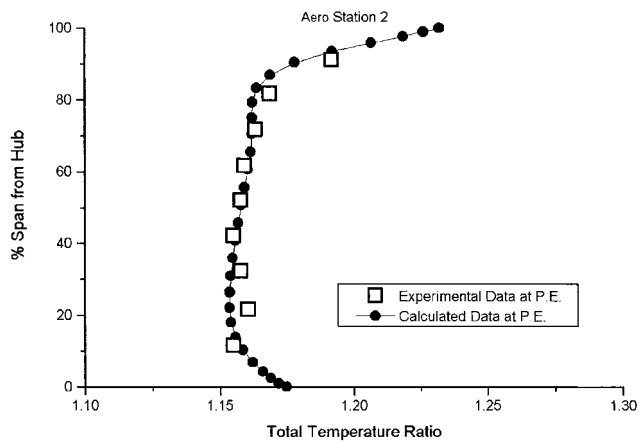

Fig. 2 Total temperature profiles at Aero Station 2

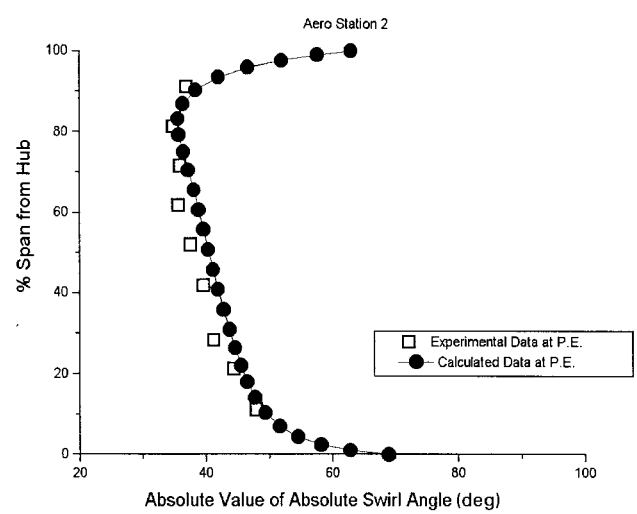

Fig. 3 Swirl angle profiles at Aero Station 2

exception of the experimental data at 100 per cent radial position. The discrepancy is thought to be mainly due to the effect of tip leakage flows, which is not modelled here. Nonetheless, the overall viscous profile is predicted to a good resemblance of the experimental profiles.

There are also good comparisons of the total temperature ratio and the absolute exit swirl angle profiles. Figure 3 shows some overestimation in the prediction of the exit flow angle. This magnitude of difference is, however, in agreement with the results obtained in references [**24**] and [**26**]. In addition, the computed Mach number contours are also verified to be in close agreement with that obtained in the experiment using laser anemometry. These are not shown here but may be found in reference [**17**].

3 DESCRIPTION OF THE INVERSE DESIGN METHOD

The design procedure consists of three main parts:

(a) the original flow solver ('analysis' mode),
(b) the modified flow solver based on a transpiration model ('design' mode),
(c) the blade update algorithm.

The bulk of the computation is carried out in the modified solver and in performing the blade updates. The blade update is carried out using the surface transpiring flow velocities such that its surfaces are realigned with the flow, thereby satisfying the tangency condition. As the iterative design procedure converges, the amount of transpiring normal flow decreases progressively, eventually giving the final blade shape.

The flowfields given by the solver in design and direct modes for the final blade design are very similar. The flow computation in direct mode is included here mainly to affirm that the finally obtained ΔP distribution coincides with the target. As illustrated in Fig. 4, the essential steps in the methodology are therefore as follows:

1. Input the initial blade geometry with fixed hub and casing surfaces.
2. Fix the flow conditions in the solver and calculate the steady flow solution.
3. Output the pressure loading ΔP^0.
4. Check if the target ΔP^* is satisfied.
   If not, necessary blade modifications are calculated and the blade is updated. The process returns to step (2) and is repeated.
   If satisfactory, the final blade geometry is obtained. Output the blade geometry to the flow solver in analysis mode to compute the final flowfield.

3.1 Theoretical background of the design algorithm

Following previous work [**5–7**], the blade surfaces, $\alpha^{\pm}$, are written as

$$\alpha^{\pm} = \theta - \left(f \pm \frac{t_\theta}{2}\right) = n\frac{2\pi}{N}, \qquad n = 1, 2, 3, \ldots, N \quad (1)$$

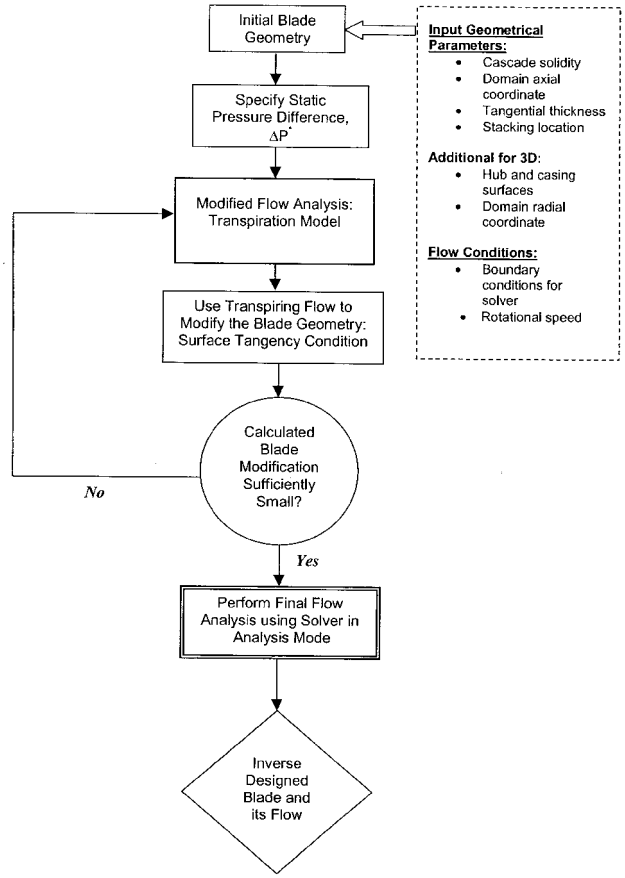

Fig. 4 Simplified flow chart of the inverse design method

where f is the mean camber line, t_θ (see Fig. 5) is the tangential thickness, $f \pm t_\theta/2$ represents the angular coordinates of points on the upper and lower surfaces of the blade, θ is the tangential coordinate of a cylindrical polar coordinate system and N is the number of blades in the cascade arrangement.

With this convention, the thickness of a blade can be based on a specified uncambered aerofoil and set off on the camber line at each chordal station to form the blade. This is in agreement with current design practice.

In the analysis mode (section 2.2), the surface flow is allowed to slip along the solid walls of the blade surfaces. Mathematically, the tangency condition can be expressed as

$$\boldsymbol{W}^{\pm} \cdot \nabla\alpha^{\pm} = 0 \quad (2)$$

where $\nabla\alpha^{\pm}$ represents the vectors normal to the blade surfaces and $\boldsymbol{W}^{\pm}$ represents the relative velocities at the upper and lower blade surfaces.

Expanding the expression separately for the upper and lower surfaces of the blade yields the following:

Upper surface

$$V_z^+ \frac{\partial f^+}{\partial z} = \frac{V_\theta^+}{r^+} - V_r^+ \frac{\partial f^+}{\partial r} - \omega \quad (3)$$

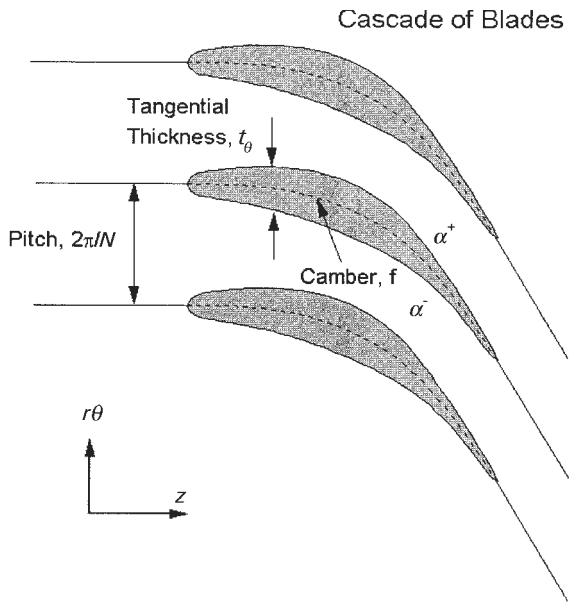

Fig. 5 Blade cascade with prescribed tangential thickness

Lower surface

$$V_z^- \frac{\partial f^-}{\partial z} = \frac{V_\theta^-}{r^-} - V_r^- \frac{\partial f^-}{\partial r} - \omega \tag{4}$$

where ω is the rotational speed.

3.2 Transpiration model

In the transpiration model, the condition given by equation (2) is not satisfied on the blade surfaces. Instead, the target surface static pressure difference distribution is imposed. This parameter is given as the difference between the pressures on the upper and lower surfaces of the blade, that is

$$\Delta P = P^+ - P^- \tag{5}$$

Denoting the target quantity as ΔP^*, the surface pressures are updated as follows:

$$(P^\pm)^{m+1} = (P_{\text{bl}})^m \pm \tfrac{1}{2}\Delta P^* \tag{6}$$

where $(P^\pm)^{m+1}$ denotes the updated upper and lower surface pressures and $(P_{\text{bl}})^m$ denotes the original value of the blade-averaged pressure defined as

$$(P_{\text{bl}})^m = \tfrac{1}{2}(P^+ + P^-)^m \tag{7}$$

with the superscripts m and $m+1$ corresponding respectively to the values before and after the target ΔP is imposed. In addition to the surface static pressure, the surface tangential velocities are also updated. This is performed using

$$(V_\theta^\pm)^{m+1} = (V_{\theta_{\text{bl}}})^m \pm \tfrac{1}{2}\Delta V_{\theta_{\text{islip}}} \tag{8}$$

where $(V_{\theta_{\text{bl}}})^m$ is the calculated blade-averaged value of the transpiring tangential velocity value (i.e. $= \frac{1}{2}[(V_\theta^+)^m + (V_\theta^-)^m]$). In this equation, $\Delta V_{\theta_{\text{islip}}}$ represents the difference between the tangential velocities on the upper and lower surfaces of the blade section. It is calculated on the basis of satisfying the tangency condition with the computed values of the axial and radial velocities, $V_z^\pm$ and $V_r^\pm$, and the current blade surface geometries. It is obtained by subtracting the expressions given in equations (3) and (4) to give

$$\Delta V_{\theta_{\text{islip}}} = \left(r^+ V_z^+ \frac{\partial f^+}{\partial z} + r^+ V_r^+ \frac{\partial f^+}{\partial r}\right) - \left(r^- V_z^- \frac{\partial f^-}{\partial z} + r^- V_r^- \frac{\partial f^-}{\partial r}\right) \tag{9}$$

which is then evaluated on the transformed (ξ, η) computational plane.

It is noted that, when the design procedure finally converges, the target blade pressure difference is fully satisfied and the flow is aligned with the surfaces of the final blade. Equations (6) and (8) then provide no change to the computed surface pressures and tangential velocities respectively. A comprehensive account of inverse principle used in aerodynamic designs may be found in reference [**27**].

3.3 Derivation of the camber line update algorithm

Computation of the new blade (or blade section) shape is performed at the end of each flow computation using the modified solver. The blade is updated by adjusting the camber shape such that the new blade surfaces are realigned with the transpiring flow. Denoting the flow quantities of the current blade with the superscript n, it follows that the new blade camber is determined by applying equations (3) and (4) (evaluated with the current values of the transpiring velocity components) and adding to give

$$\begin{aligned}(V_z^+ + V_z^-)^n \frac{\partial f^{n+1}}{\partial z} + \frac{(V_z^+ - V_z^-)^n}{2}\frac{\partial t_\theta}{\partial z} \\ + (V_r^+ + V_r^-)^n \frac{\partial f^{n+1}}{\partial r} + \frac{(V_r^+ - V_r^-)^n}{2}\frac{\partial t_\theta}{\partial r} \\ = \left[\frac{(V_\theta^+)^{m+1}}{r^+} + \frac{(V_\theta^-)^{m+1}}{r^-}\right]^n - 2\omega\end{aligned} \tag{10}$$

where f^{n+1} is the new camber geometry of the blade whose surfaces are parallel to the surface transpiring velocity vectors.

Using subscript 'bl' to represent the blade-averaged value, notation Δ to denote the blade difference value and replacing r^+ and r^- by r (since $r^+ = r^-$ in the vertical H-grid

topology), the final expression for the blade update algorithm becomes

$$V^n_{z_{\mathrm{bl}}}\frac{\partial f^{n+1}}{\partial z}+V^n_{r_{\mathrm{bl}}}\frac{\partial f^{n+1}}{\partial r}=\left(\frac{V^n_{\theta_{\mathrm{bl}}}}{r}-\omega\right)-\frac{1}{4}\Delta V^n_z\frac{\partial t_\theta}{\partial z}-\frac{1}{4}\Delta V^n_r\frac{\partial t_\theta}{\partial r} \tag{11}$$

The integration is carried out in a transformed meridional plane of quasi-streamlines (ξ = constant lines) and quasi-orthogonals (η = constant), starting from the stacking line, given as a fixed camber angle along a chosen quasi-orthogonal position. The final expression for the blade update equation in the (ξ, η) plane is then

$$f^{n+1}_\eta+\frac{V^n_{\xi_{\mathrm{bl}}}}{V^n_{\eta_{\mathrm{bl}}}}f^{n+1}_\xi=\frac{J}{V^n_{\eta_{\mathrm{bl}}}}\left(\frac{V^n_{\theta_{\mathrm{bl}}}}{r}-\omega\right)-\frac{1}{4V^n_{\eta_{\mathrm{bl}}}}(\Delta V^n_\xi t_{\theta_\xi}+\Delta V^n_\eta t_{\theta_\eta}) \tag{12}$$

where $V_{\xi_{\mathrm{bl}}}$ and $V_{\eta_{\mathrm{bl}}}$ are the vertical and horizontal velocity components respectively in the transformed plane.

3.4 Treatment for surface flow separation

The velocity terms are actual values along the surfaces of the blade, but it is noted that, in the undesirable case when the design specification results in a large region of surface flow separation, equation (12) breaks down. In such cases, the program code warns the user of unsatisfactory design specification and seeks the nearest geometry by taking mass-averaged values of the horizontal component of the velocities (i.e. $\Delta\tilde{V}_\eta$, $\tilde{V}_{\eta_{\mathrm{bl}}}$) instead of the original surface values (i.e. ΔV_η, $V_{\eta_{\mathrm{bl}}}$).

3.5 Convergence criterion

In the context of the design, convergence is obtained when the blade changes become sufficiently small, indicating that the surface normal transpiring flow velocities have almost disappeared. The tolerance on the blade changes is set with respect to the axial chord length. A typical value of 0.1 per cent axial chord length is generally found to be adequate for the current applications, as demonstrated in the next section.

4 RESULTS

4.1 Validation: reproducing the fan blade

The computed pressure loading distribution across the entire meridional plane of the rotor is shown in Fig. 6. For the validation, the distribution is imposed as the design specification in the design code and the objective is to reproduce the original blade starting with a different geometry.

The left of the figure shows the final result of the computation where the blade shapes are compared at three blade heights: near the hub, at mid-span and near the tip. In each of the three plots, the initial (dashed line), the target (solid line) and the final profile (dots) are shown. At all three span positions, it can be observed that the reproduced geometry matches the original shape closely. The results therefore verify the accuracy of the algorithm.

4.2 Redesign of NASA rotor 67

Attempts are then made to modify the original rotor 67 fan blade using the proposed procedure. The pressure loading distribution of the original blade and the relative Mach number contours at three blade heights are shown in Fig. 7. It is noted that, near the tip region where there is strong shock formation across the passage, the pressure loading shows large variation. Also, in the region near the hub, the high flow incidence is reflected by the high leading-edge loading.

Two redesigns are performed. The first, FD3D-R1, is specified to have a completely aft-loaded characteristic, while the second, FD3D-R2, is chosen to give a fore-loaded characteristic at the hub of the blade and a middle-loaded characteristic from the mid-span to the tip location. The target ΔP distributions are shown in Fig. 8.

It is noted that the redesign ΔP specifications shown here have been checked in the computation finally to give a net change in the mass-averaged swirl velocity, i.e. $(r\tilde{V}_{\theta_{\mathrm{TE}}}-r\tilde{V}_{\theta_{\mathrm{LE}}})$, that matches the value obtained by the original cascade to within 1 per cent. This is achieved by varying the total area under the distribution several times before the required $(r\tilde{V}_{\theta_{\mathrm{TE}}}-r\tilde{V}_{\theta_{\mathrm{LE}}})$ is obtained by the final designs. The work capacities in the new designs are therefore consistent with the original fan.

4.3 Overview of the aerodynamic changes

4.3.1 High flow incidence at the hub

The main undesirable flow phenomenon near the hub region of the original blade is the presence of flow recirculation at the inlet (see topmost plots in Fig. 9). This is a direct consequence of having a highly loaded inlet region, which, in terms of the flow aerodynamics, gives rise to a high incidence flow near the hub of the blade. The redesigns reduce the high positive incidence flow directly by alleviating the load through a decreased ΔP value at the leading edge. The recovery of a smooth flow at the inlet is immediately achieved as shown in velocity vector plots at the bottom of the figure.

4.3.2 Mach number and shock formation

Near the blade tip, the flow aerodynamics present a different design difficulty. Here, the flow is predominantly transonic and the development of the supersonic region and shock formation in the flow passage is the main concern.

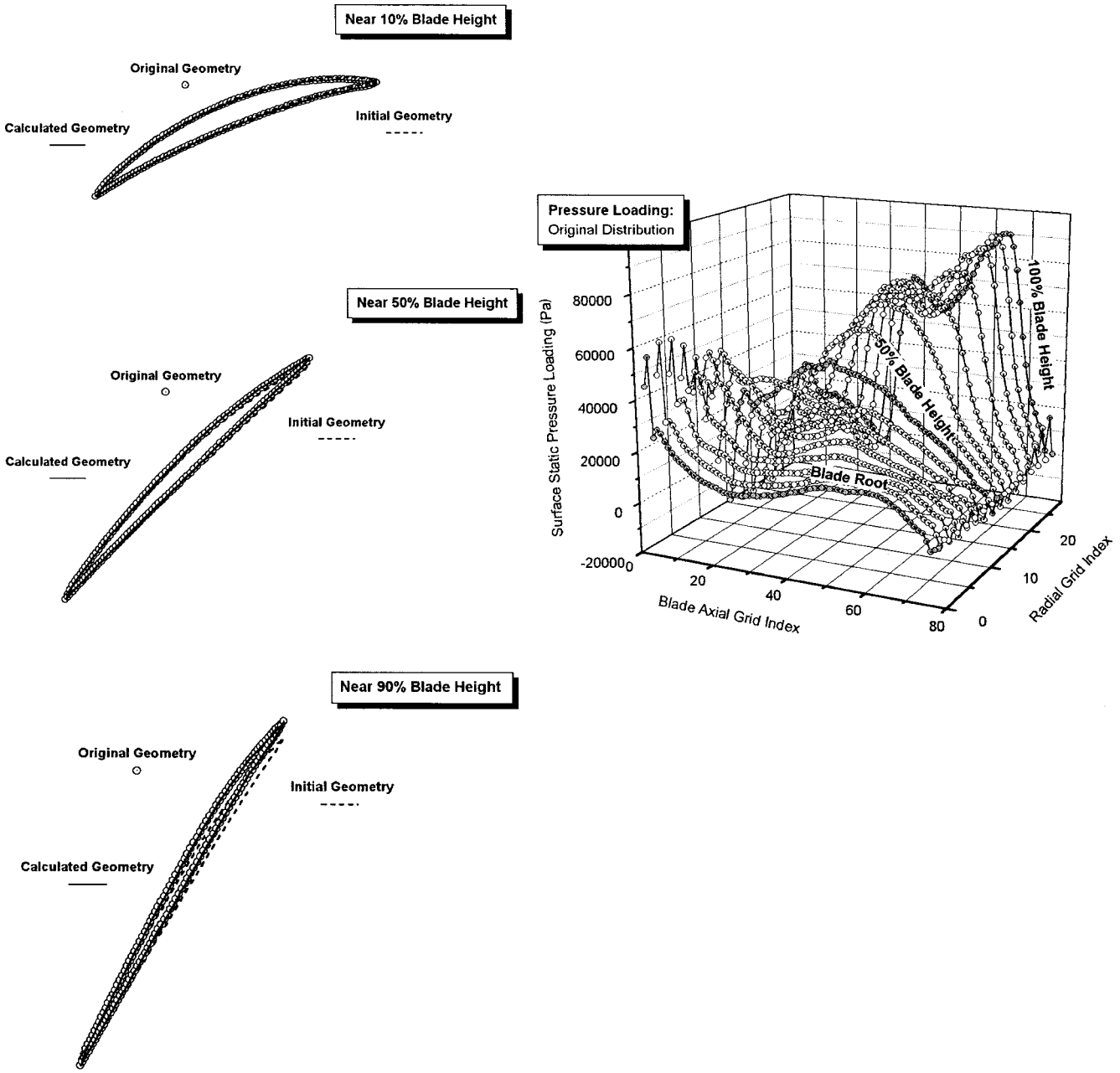

Fig. 6 Validation of three-dimensional method 2: target surface static pressure loading distributions and reproducing the fan blade

At the tip of the original blade, the shock formation near the trailing edge is at its worst and is sufficient to cause flow separation along the suction surface at the position just after the shock (see Figs 10 and 11). It is interesting to note that the effects of the shock are registered separately on the loading distribution (see leftmost plot of Fig. 10); the first trough in ΔP corresponds to the shock on the pressure side, and the second corresponds to that on the suction side of the blade.

In the first redesign, the static pressure loading in the front half of the blade axial chord is increased to give a smoothed rear-loaded characteristic at the tip. This gives rise mainly to a smoothed surface pressure distribution on the pressure side of the blade (see bottom left-hand plot of Fig. 10). In terms of shock formation, the smoothed surface pressure distribution corresponds to the pressure leg of the shock formation being weakened considerably (note also that the pressure distributions as computed by the solver in the final design and analysis modes match almost exactly). This is represented by the diffused Mach number contours shown in the top middle plot of the figure.

In design FD3D-R2, the specified pressure loading is middle-loaded along the blade tip. With this distribution, the abrupt changes in the original ΔP distribution that correspond to the pressure and suction legs of the passage shock

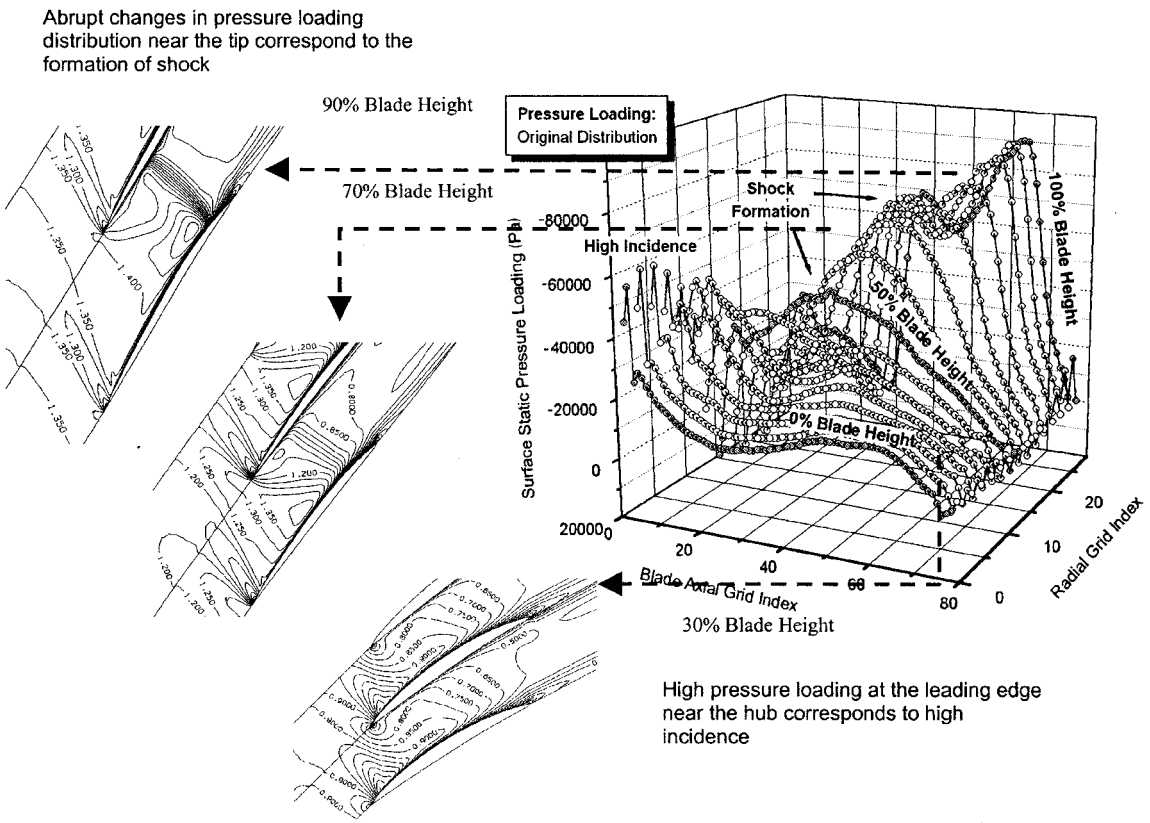

Fig. 7 Original ΔP distribution (with relative Mach number contours at three blade heights)

in the original cascade are replaced by a gentle variation (see bottom right-hand plot in Fig. 10). In this case, the shock weakening takes place on both sides of the blade, as may be observed in the Mach number contours of design FD3D-R2, given in the top rightmost plot of Fig. 10. The velocity vectors in the trailing-edge region at the blade tip of the three blades are shown in Fig. 11.

In design FD3D-R1, the flow near the trailing edge no longer separates, but a small region of flow diffusion can still be observed on the suction side (see middle plot of

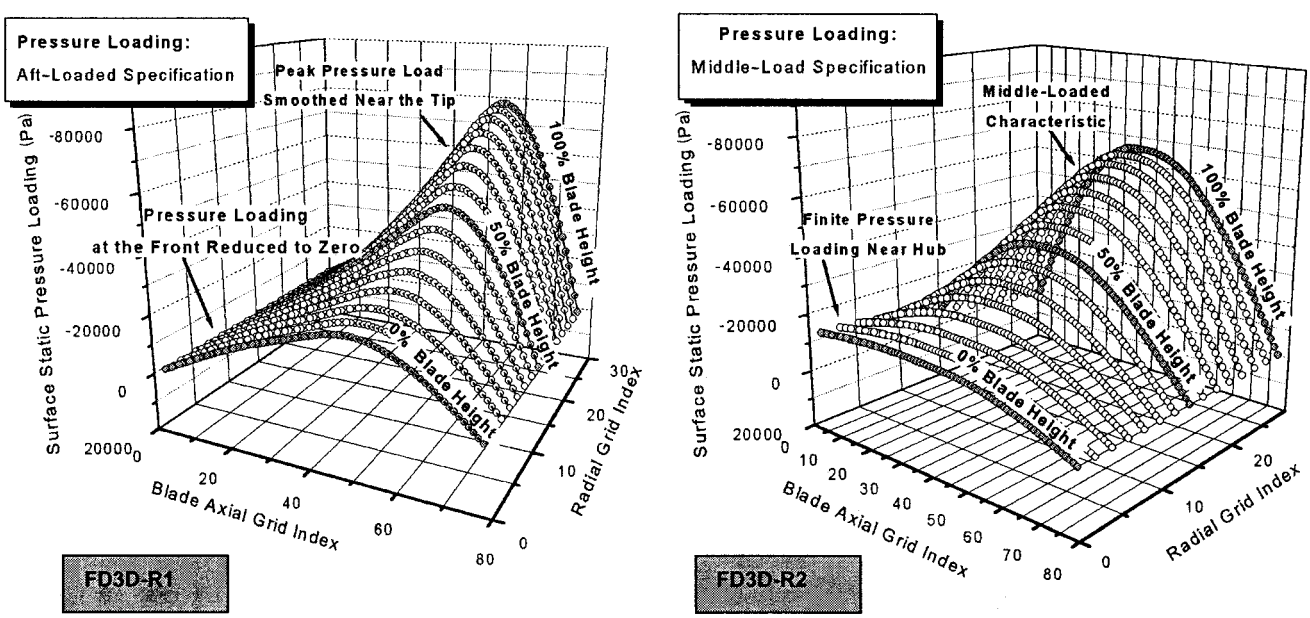

Fig. 8 Redesign specifications: FD2D-R1 (aft-loaded) and FD2D-R2 (fore/middle-loaded)

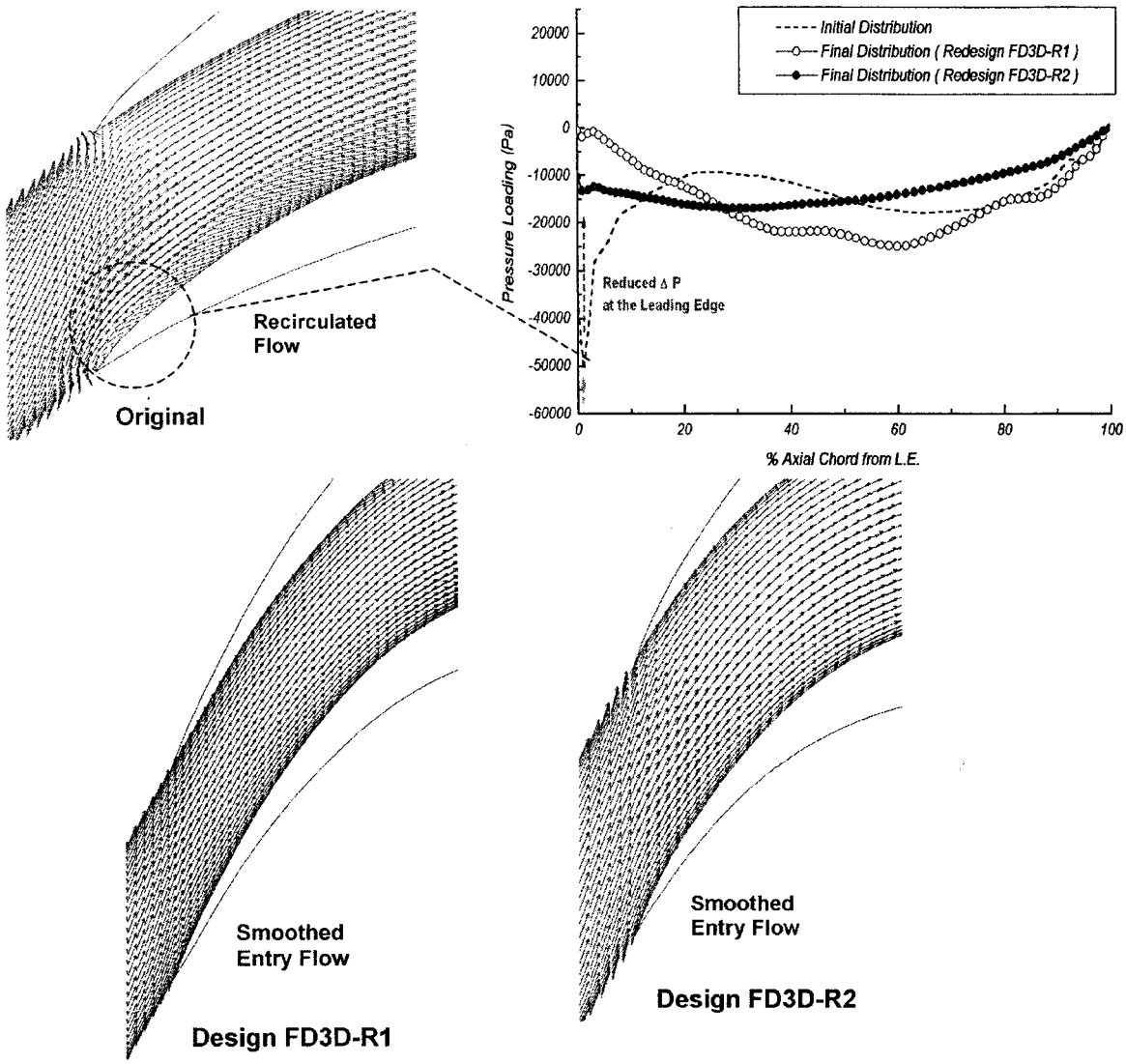

Fig. 9 Pressure loading distributions with corresponding relative velocity vectors at the hub for the original fan and the redesigns

Fig. 11). This is caused by the suction leg of the shock formation, which is allowed to remain in this redesign by its specified ΔP. In the second redesign, however, with the shock formation weakened at both surfaces of the blade, the shock–boundary layer interaction is reduced, thereby giving a smoothed surface flow in the final FD3D-R2 blade (see rightmost plot of Fig. 11).

In terms of loss, a substantial amount of entropy is generated across the normal shock in the original blade. In design FD3D-R1, there is still a distinct band of concentrated entropy generation across the position of the shock. However, the thermodynamic irreversibility is noticeably less, especially on the pressure side of the blade where the pressure leg of the passage shock has been weakened (see middle plot in Fig. 12). The rightmost plot shows no obvious concentration of entropy generation as a result of the substantially weakened shock in design FD3D-R2.

The entropy generation contours at the mid-pitch position in the meridional view are shown in Fig. 13. Here, it may again be observed that the entropy generation in design FD3D-R2 is the least intense among the three blades.

4.3.3 Performance maps: original and redesigned fans

Figures 14 and 15 show the adiabatic efficiencies and total pressure ratios of the original and redesigned blades plotted against the computed mass flowrate, which is normalized with respect to the choked mass flowrate of the original fan. The maps compare the performance of the three blades. The numerical performance characteristics of the original blade and those of design FD3D-R2 are represented by the solid circle line and solid square line respectively, while that of FD3D-R1 is denoted by the solid line with smaller squares.

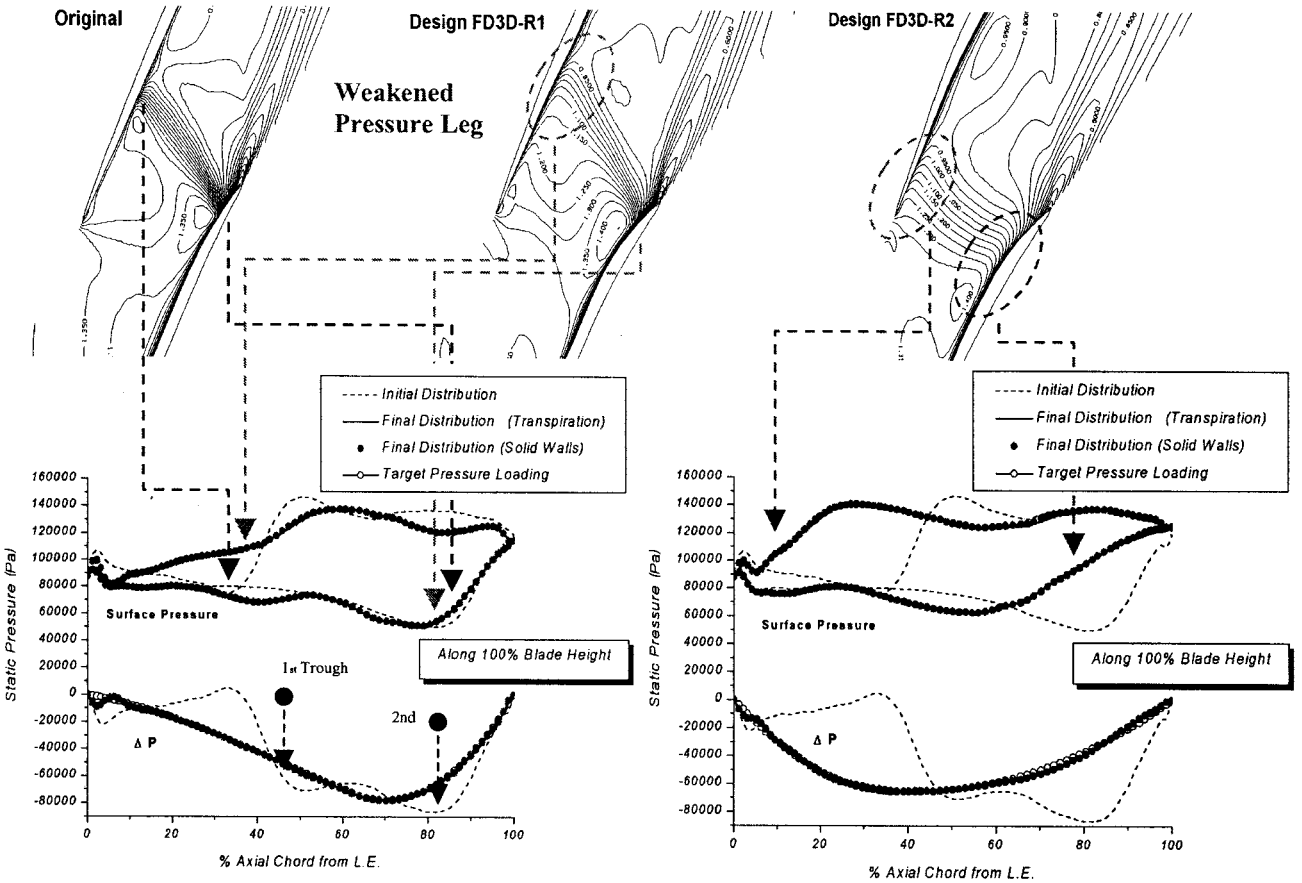

Fig. 10 Relative Mach number contours at the tip for the original fan and designs FD3D-R1 and FD3D-R2 (showing relationships to the static pressure distributions)

In terms of adiabatic efficiency, an improvement is achieved by design FD3D-2D, where a small increase (about 0.6 per cent at the design point) can be observed over most of the working range. On the other hand, the first redesign does not seem to yield any improvement. Also, it is noted that, particularly in the first design, FD3D-R1, although the shock near the tip is weakened moderately, the shock formation has extended across the span as indicated by the dotted lines in Fig. 13. This has given rise to a lower choke flow as given in the operating characteristics (Figs 14 and 15) in the next section.

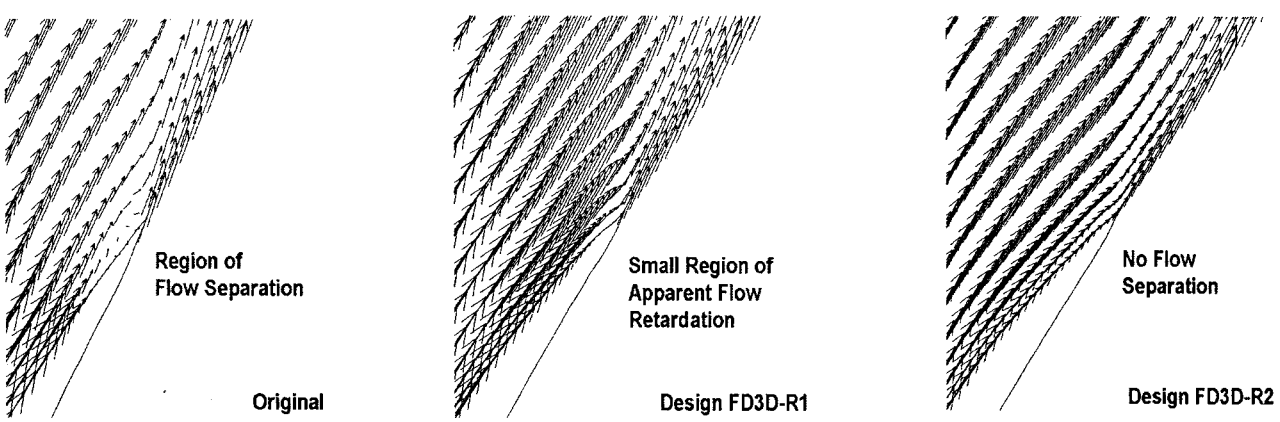

Fig. 11 Relative velocity vectors near the trailing edge at the tip for the original fan and designs FD3D-R1 and FD3D-R2

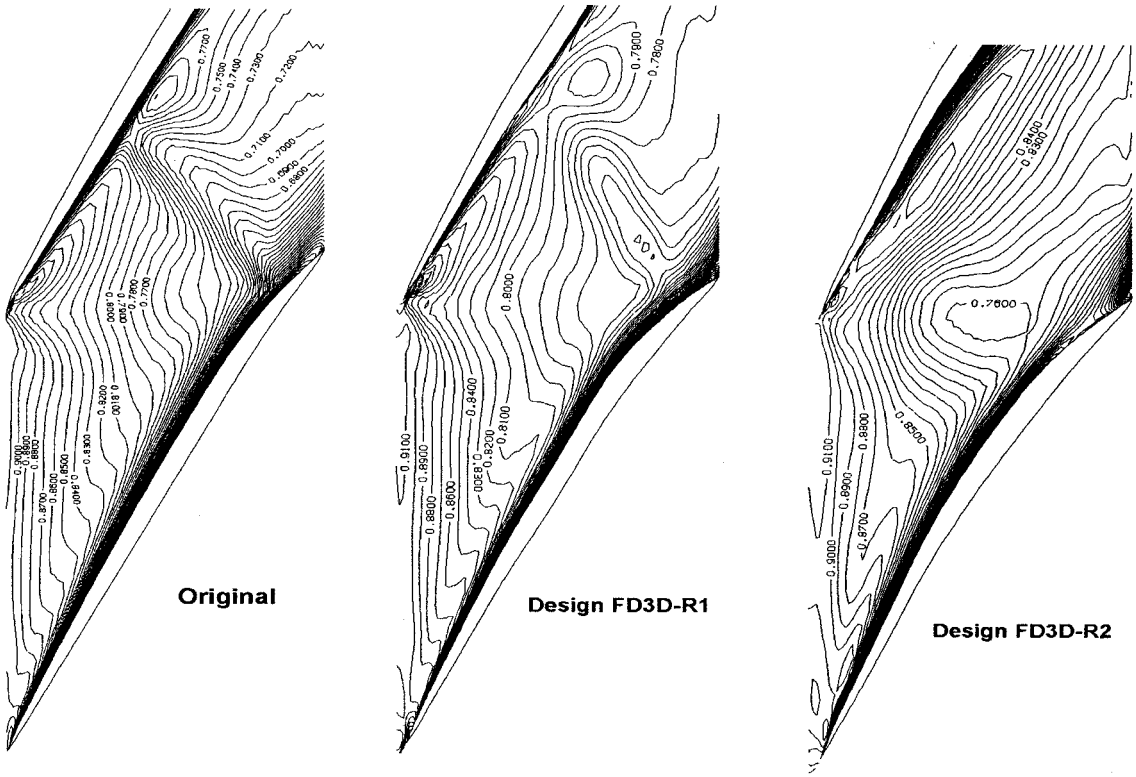

Fig. 12 Contours of entropy generation, $\exp(-\Delta S/R)$, at the tip for the original fan and designs FD3D-R1 and FD3D-R2 (contour interval 0.01)

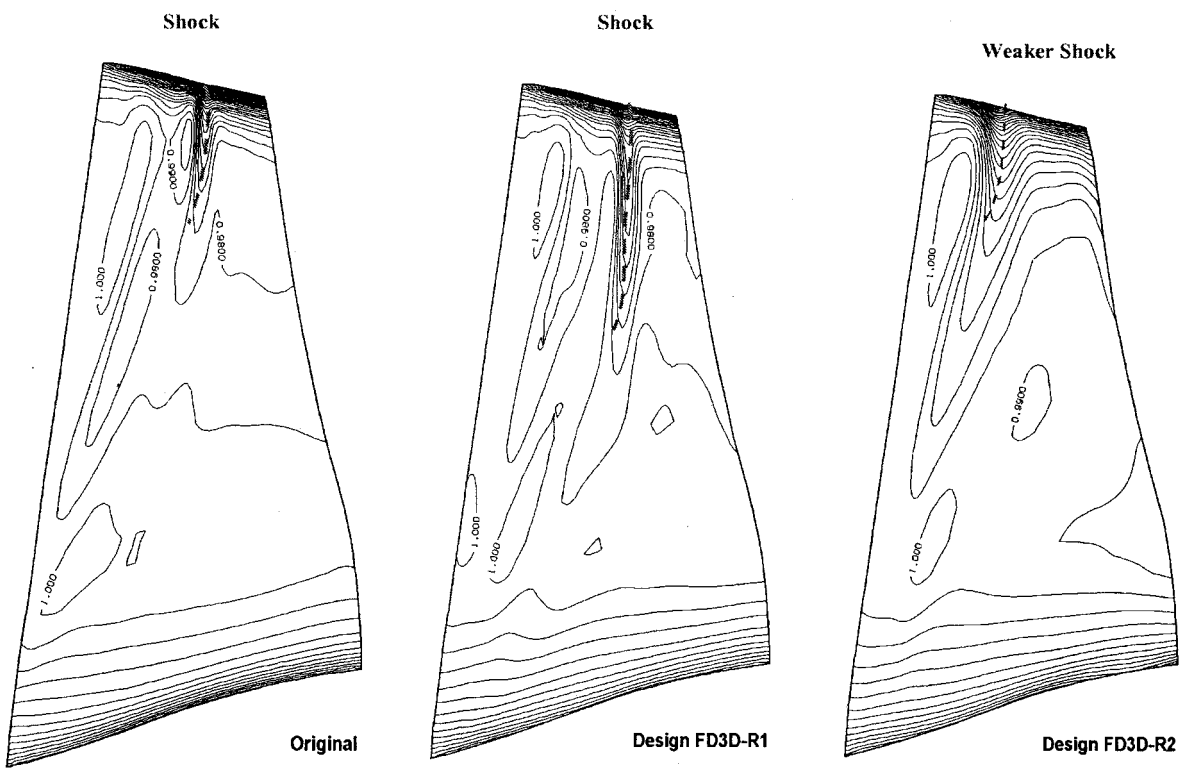

Fig. 13 Contours of entropy generation, $\exp(-\Delta S/R)$, at the mid-pitch for the original fan and designs FD3D-R1 and FD3D-R2 (contour interval 0.01)

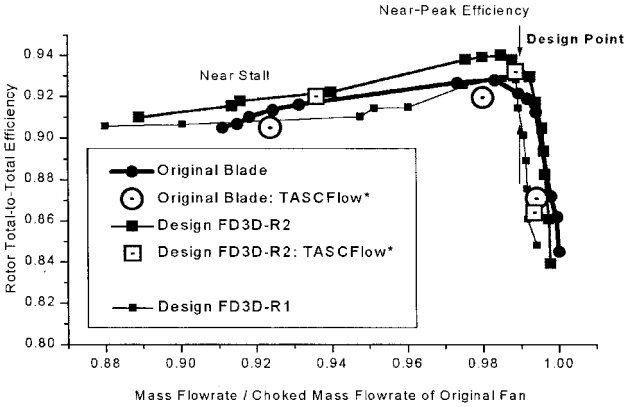

Fig. 14 Adiabatic efficiency for the original fan and designs FD3D-R1 and FD3D-R2 (*commercial Navier–Stokes solver code)

In terms of total pressure ratios, the operating maps of the three blades are very similar, with the redesigns retaining the trend of increasing pressure ratios as mass flowrate is lowered. Comparing the characteristics of design FD3D-R2 with those of the original fan, there is only a marginal increase in the total pressure ratio delivered by the new fans.

The operating lines for design FD3D-R2 and the original fan in relation to each other are checked using a commercial code—TASCFlow (version 2.9)—which solves the Navier–Stokes equations on the basis of an implicit scheme and uses the standard κ–ε turbulence model to account for flow turbulence. The commercial code is used to provide three points of comparison on the maps for both the original and redesigned FD3D-R2 blades; these points are represented by the open circle and square legends respectively. As shown in the two figures, the relative position of the points computed by the commercial code for the two blades is in agreement with that indicated by the present code.

Besides an increased efficiency, the FD3D-R2 blade has an increased working range. In fact, the stall margins

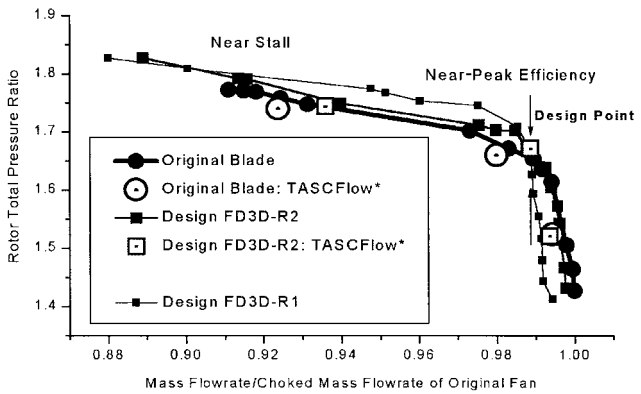

Fig. 15 Total pressure ratio for the original fan and designs FD3D-R1 and FD3D-R2

$(\dot{m}_{ratio_{choke}}/\dot{m}_{ratio_{stall}})$ of both the new blades are higher at 1.130 and 1.122 for designs FD3D-R1 and FD3D-R2 respectively, compared with 1.089 for the original blade. This is understood to be mainly due to the improvement made on the poor incidence flow near the hub of the original blade. As the high positive incidence near the leading edge is reduced in the two redesigns, there is increased tolerance to the development of stall as the mass flowrate is reduced. This explains the larger operating margin of design FD3D-R1 as compared with design FD3D-R2, with the former having an incidence angle of less than half that in the latter at the design point.

5 CONCLUDING REMARKS

Two redesigns of the NASA rotor 67 fan blade were performed using the proposed methodology. Design efforts concentrated on improving the poor incidence near the hub and strong shock formation near the tip by changing the static pressure loading characteristics. An overall qualitative improvement in the flow aerodynamics was made. The operating maps of both redesigns show that they have larger working ranges, and the new design FD3D-R2, which has a substantially reduced shock formation near its tip, gives an efficiency about 0.6 per cent higher than that of the original fan at the design point. The improvement in the efficiency of design FD3D-R2 is confirmed by the computational results given by the commercial Navier–Stokes solver TASCFlow (version 2.9). The extension of the current method to the suppression of secondary flow in centrifugal pumps is now in progress.

ACKNOWLEDGEMENT

The authors are thankful to Ebara Research Company Limited for providing financial and technical support to the work presented.

REFERENCES

1 **Casey, M. V.** The industrial use of CFD in the design of turbomachinery. AGARD Lecture Series 195, 1994.
2 **Demeulenaere, A.** and **Van Den Braembussche, R. A.** Three-dimensional inverse method for turbomachinery blading design. ASME paper 96-GT-39, 1996.
3 **Dulikravich, G. S.** and **Baker, D. P.** Aerodynamic shape inverse design using a Fourier series method. AIAA paper 99-0185, 1999.
4 **Wang, Z., Cai, R., Chen, H.** and **Zhang, D.** A fully three-dimensional inverse method for turbomachinery blading with Navier–Stokes equations. Presented at the International Gas Turbine and Aeroengine Congress and Exhibition, 2–5 June 1998, ASME paper 98-GT-126, 1998.
5 **Hawthorne, W. R., Tan, C. S., Wang, C.** and **McCune, J.** Theory of blade design for large deflections. Part 1: Two

dimensional cascades. *J. Engng for Gas Turbine and Power*, 1984, **106**, 346–353.

6 **Tan, C. S., Hawthorne, W. R., McCune, J. E.** and **Wang, C.** Theory of blade design for large deflection. Part 2: annular cascades. *J. Engng for Gas Turbines and Power*, 1984, **106**, 355–365.

7 **Zangeneh, M.** A compressible three-dimensional design method for radial and mixed flow turbomachinery blades. *Int. J. Numer. Meth. In Fluids*, 1991, **13**, 599–624.

8 **Zangeneh, M., Goto, A.** and **Harada, H.** On the design criteria for suppression of secondary flows in centrifugal and mixed flow impellers. ASME paper 97-GT-393, 1997.

9 **Ashihara, K.** and **Goto, A.** Improvements of pump suction performance using 3D inverse design method. ASME paper FEDSM99-6846, 1999.

10 **Yiu, K. F. C.** and **Zangeneh, M.** On the simultaneous design of blade and duct geometry of marine ducted propulsors. *J. Ship Res.*, 1998, **42**(4), 274–296.

11 **Black, S. D.** Integrated lifting-surface/Navier–Stokes design and analysis methods for marine propulsors. PhD thesis, Massachusetts Institute of Technology, 1997.

12 **Demeulenaere, A., Leonard, O.** and **Van Den Braembussche, R. A.** A two dimensional Navier–Stokes inverse solver for compressor and turbine blade design. *Proc. Instn Mech. Engrs, Part A, J. Power and Energy*, 1997, **211**, 299–307.

13 **Tiow, W. T.** and **Zangeneh, M.** A three-dimensional viscous transonic inverse design method. Presented at the International Gas Turbine and Aeroengine Congress and Exhibition, 8–11 May 2000, ASME paper 2000-GT-525, 2000.

14 **Tiow, W. T.** and **Zangeneh, M.** A viscous transonic inverse design method for turbomachinery blades. Part 1: 2D cascades. Presented at the International Gas Turbine and Aeroengine Congress and Exhibition, 2–5 June 1998, ASME paper 98-GT-125, 1998.

15 **Dang, T.** Inverse method for turbomachine blades using shock-capturing techniques. AIAA paper 95-2465, 1995.

16 **Ahmadi, M.** and **Ghaly, W. S.** Aerodynamic design of turbomachinery cascades using a finite volume method on unstructured meshes. In Proceedings of 5th Conference of CFD Society of Canada CFD-97, 1997, pp. 2-15–2-21.

17 **Tiow, W. T.** Inverse design of turbomachinery blades in rotational flow. PhD thesis, University College, University of London, 2000.

18 **Qiu, X.** and **Dang, T.** 3D inverse method for turbomachine blading with splitter blades. Presented at the International Gas Turbine and Aeroengine Congress and Exhibition, 8–11 May 2000, ASME paper 2000-GT-0526, 2000.

19 **Hall, M. G.** Cell-vertex multigrid schemes for solution of the Euler equations. In Conference on *Numerical Methods for Fluid Dynamics* (Eds K. W. Morton and M. J. Baines), Reading, Berkshire, 1986.

20 **Jameson, A., Schmidt, W.** and **Turkel, E.** Numerical solutions of the Euler equations by finite volume method using Runge Kutta time stepping schemes. AIAA paper 8l-l259, 1981.

21 **Denton, J. D.** The use of a distributed body force to simulate viscous effects in 3D flow calculations. ASME paper 86-GT-144, 1986.

22 **Denton, J. D.** The calculation of three dimensional viscous flow through multistage turbomachines. ASME paper 90-GT-19, 1990.

23 Test cases for computation of internal flows in Aero Engine components. AGARD Advisory Report 275, 1985.

24 **Jennions, I. K.** and **Turner, M. G.** Three-dimensional Navier Stokes computations of transonic fan flow using an explicit flow solver and an implicit κ–ε solver. *J. Turbomach.*, 1993, **115**, 261–272.

25 **He, L.** and **Denton, J. D.** Three-dimensional time-marching inviscid and viscous solutions for unsteady flows around vibrating blades. *J. Turbomach.*, 1994, **116**, 469–476.

26 **Arnone, A.** Viscous analysis of three dimensional rotor flow using multigrid method. *J. Turbomach.*, 1994, **116**, 435–445.

27 **Yiu, K. F. C.** and **Stow, P.** Aspects of the transpiration model for airfoil design. *Int. J. Numer. Meth. in Fluids*, 1994, **18**, 509–528.